








# The Slow Heartbeats of an Ultraluminous X-Ray Source in NGC 3621

S. E. Motta<sup>1,2</sup>, M. Marelli<sup>3</sup> , F. Pintore<sup>3</sup>, P. Esposito<sup>3,4</sup> , R. Salvaterra<sup>3</sup> , A. De Luca<sup>3,5</sup>, G. L. Israel<sup>6</sup>, A. Tiengo<sup>3,4,5</sup> , and G. A. Rodríguez Castillo<sup>6</sup> 

<sup>1</sup> Department of Physics, Astrophysics, University of Oxford, Denys Wilkinson Building, Keble Road, OX1 3RH Oxford, UK; [sara.motta@physics.ox.ac.uk](mailto:sara.motta@physics.ox.ac.uk)

<sup>2</sup> INAF–Osservatorio Astronomico di Brera, via E. Bianchi 46, I-23807 Merate (LC), Italy

<sup>3</sup> INAF–Istituto di Astrofisica Spaziale e Fisica Cosmica di Milano, via A. Corti 12, I-20133 Milano, Italy

<sup>4</sup> Scuola Universitaria Superiore IUSS Pavia, Palazzo del Broletto, piazza della Vittoria 15, I-27100 Pavia, Italy

<sup>5</sup> INFN, Sezione di Pavia, Via A. Bassi 6, I-27100 Pavia, Italy

<sup>6</sup> INAF–Osservatorio Astronomico di Roma, via Frascati 33, I-00078 Monteporzio Catone, Italy

Received 2020 May 10; revised 2020 June 5; accepted 2020 June 9; published 2020 August 5

## Abstract

We report on the results of X-ray observations of 4XMM J111816.0–324910, a transient ultraluminous X-ray source located in the galaxy NGC 3621. This system is characterized by a transient nature and marked variability with a characteristic timescale of  $\approx 3500$  s, in contrast with other ultraluminous X-ray sources, which in the vast majority show limited intra-observation variability. Such a behavior is very reminiscent of the so-called heartbeats sometimes observed in the Galactic black hole binary GRS 1915+105, where the variability timescale is  $\sim 10$ –1000 s. We study the spectral and timing properties of this object and find that overall, once the differences in the variability timescales are taken into account, they match quite closely those of both GRS 1915+105 and of a number of objects showing heartbeats in their light curves, including a confirmed neutron star and a supermassive black hole powering an active galactic nucleus. We investigate the nature of the compact object in 4XMM J111816.0–324910 by searching for typical neutron star signatures and by attempting a mass estimate based on different methods and assumptions. Based on the current available data, we are not able to unambiguously determine the nature of the accreting compact object responsible for the observed phenomenology.

*Unified Astronomy Thesaurus concepts:* Black holes (162); Neutron stars (1108); Accretion (14); X-ray point sources (1270); Compact objects (288); Extragalactic astronomy (506)

## 1. Introduction

The detection and characterization of X-ray variability play a role of paramount importance in the process of identifying the nature of a source and studying the mechanisms powering the observed emission. In accreting sources, it offers unique insights into the condition of disks, accretion flows, winds, and jets in the extreme environments surrounding a compact object. In this work, we investigate a peculiar X-ray source in the galaxy NGC 3621, listed in the 4XMM catalog (Webb et al. 2020) as 4XMM J111816.0–324910 (hereafter 4X J1118). This source was singled out due to its marked variability during a large study of the soft X-ray sky in the temporal domain, carried out via tools developed as part of the EXTras project,<sup>7</sup> which were applied to all the XMM-Newton observations performed up to the end of 2018.

NGC 3621 is a spiral galaxy located at a Cepheid distance of 6.7 Mpc (Tully et al. 2013). Despite the bulgeless morphology of NGC 3621, Satyapal et al. (2007) discovered a faint active galactic nucleus (AGN) in its nuclear cluster from mid-infrared observations and, based on estimates of its bolometric luminosity, set a lower limit on the mass of the central black hole (BH) of  $4 \times 10^3 M_{\odot}$ . Barth et al. (2009) classified NGC 3621 as a Seyfert 2 galaxy based on its optical spectrum, and from stellar-dynamical modeling of the nuclear cluster set an upper limit to the BH mass of  $3 \times 10^6 M_{\odot}$ . Using a Chandra observation performed in 2008 March, Gliozzi et al. (2009) found further evidence for an AGN in NGC 3621 with the

detection of a weak X-ray point source coincident with the nucleus.

In the same observation, they also detected two bright off-nucleus sources (one in the ultraluminous X-ray source (ULX; Kaaret et al. 2017) regime) but did not focus on 4X J1118, which at the time was at the inconspicuous luminosity of  $L_X \approx 10^{37}$  erg s<sup>-1</sup> (see Section 4), yielding only a handful of photons. In a more recent XMM-Newton observation (taken in 2017 December), we detected 4X J1118 at more than  $3 \times 10^{39}$  erg s<sup>-1</sup>, which qualifies it as a new (transient) ULX.<sup>8</sup> Even more surprisingly, the inspection of its light curve revealed an unusual quasi-periodic modulation of the flux, very reminiscent of that seen at times in the Galactic BH X-ray binary GRS 1915+105, the so-called heartbeat oscillations (formally known as  $\rho$ -class variability, according to the classification proposed by Belloni et al. 2000).

In the following, we report on the timing and spectral characteristics of 4X J1118, based on the XMM-Newton observation and discuss the nature of this very peculiar source, also using data from Chandra, the Swift Neil Gehrels Observatory, NuSTAR, and Hubble Space Telescope (HST).

## 2. XMM-Newton Observation, Data Reduction, and Analysis

The XMM-Newton observation that showed 4X J1118 as a ULX (see Table 1) comprises data from both EPIC-pn and the EPIC-MOS1 and MOS2 CCD cameras. Because of the low flux and complicated field, the RGS did not provide useful data.

<sup>7</sup> Exploring the X-ray Transient and variable Sky (De Luca et al. 2016) was a project aimed at mining the XMM-Newton archival data for periodic and aperiodic variability in the time domain at all timescales (limited to the 3XMM-DR5 catalog observations; Rosen et al. 2016). See <http://www.extras-fp7.eu>.

<sup>8</sup> We note that also the fainter nonnuclear source studied by Gliozzi et al. (2009), their “source C,” was above the ULX threshold in the same XMM-Newton observation.

**Table 1**  
Journal of the X-Ray Observations of 4X J1118

Instrument	Obs.ID	Date	Exposure (ks)	Count Rate (Counts s <sup>-1</sup> )
Chandra/ACIS-S	9278	2008 Mar 6	21.2	$(7.5 \pm 2.7) \times 10^{-4}$
Swift/XRT	00045607001	2011 Aug 1	0.9	$<1.3 \times 10^{-2}$
Swift/XRT	00045607002	2011 Aug 2	3.8	$<8 \times 10^{-3}$
Swift/XRT	00045607003	2011 Aug 4	2.0	$<1.1 \times 10^{-2}$
Swift/XRT	00045607004	2011 Aug 5	2.5	$<9 \times 10^{-3}$
Swift/XRT	00045607005	2011 Aug 8	0.3	$<4.2 \times 10^{-2}$
Swift/XRT	00045607006	2011 Aug 10	0.4	$<3.8 \times 10^{-2}$
Swift/XRT	00045607007	2011 Aug 14	3.9	$<9 \times 10^{-3}$
Swift/XRT	00045607008	2012 Aug 12	4.6	$<6 \times 10^{-3}$
Swift/XRT	00045607009	2012 Aug 14	6.0	$<6 \times 10^{-3}$
Swift/XRT	00045607010	2012 Aug 15	3.3	$<8 \times 10^{-3}$
Swift/XRT	00045607011	2012 Aug 17	2.9	$<1.2 \times 10^{-2}$
Swift/XRT	07006864001	2017 Feb 28	0.1	$<0.28$
Swift/XRT	07006862001	2017 Mar 10	0.1	$<0.27$
Swift/XRT	07006864002	2017 Mar 15	0.5	$<2.6 \times 10^{-2}$
Swift/XRT	00088212001	2017 Dec 15	1.1	$<5.4 \times 10^{-2}$
NuSTAR/FPM A+B	60371002002	2017 Dec 15	30.8	$(4.5 \pm 0.4) \times 10^{-3}$
XMM-Newton/pn	0795660101	2017 Dec 16	33.7	$0.135 \pm 0.002$
XMM-Newton/MOS1	0795660101	2017 Dec 16	34.9	$0.041 \pm 0.001$
XMM-Newton/MOS2	0795660101	2017 Dec 16	34.9	$0.040 \pm 0.001$
Swift/XRT	00088212002	2017 Dec 20	0.9	$<1.3 \times 10^{-2}$

**Note.** The count rates are in the 0.3–10 keV energy range, except for NuSTAR, for which we used the 3–15 keV energy range. Uncertainties are at the  $1\sigma$  confidence level, upper limits are at  $3\sigma$ .

All cameras were operated in *Full-Frame* mode, which yields data with a time resolution of 73.4 ms for the EPIC-pn, 2.7 s for the MOS1, and 2.6 s for the MOS2. The data reduction was performed following standard procedures using SAS v.16.1. We selected events with  $\text{PATTERN} \leq 4$  and  $\text{PATTERN} \leq 12$  for the pn and the MOS, respectively. Photons for both the timing and spectral analysis were extracted in a circular regions with radius of  $15''$  centered on 4X J1118 (this small radius,  $\sim 70\%$  enclosed energy fraction, is due to the presence of nearby sources), while the background was evaluated from a larger source-free region in the same chip as 4X J1118. In the following, we only considered events collected when the EPIC-pn and MOS cameras were observing the target at the same time (approximately 35 ks).

### 2.1. Timing

We created three light curves of 4X J1118 by combining events collected with EPIC-pn, EPIC-MOS1, and EPIC-MOS2 in the energy bands 0.3–10, 0.3–2, and 2–10 keV. We then binned the data in three light curves with a 120 s time bin (Nyquist frequency  $N_y = 0.0083$  Hz), which corresponds to our final time resolution. In order to obtain the best possible frequency resolution ( $\delta\nu = 1/T \approx 3 \times 10^{-5}$  Hz), we calculated one single power density spectrum (PDS) from the entire light-curve extracted in the 0.3–10 keV energy band (duration  $T_{\text{obs}} \approx 34$  ks). The resulting light curve and PDS are shown in Figure 1 (top and bottom panels, respectively).

The EPIC light curve from 4X J1118 clearly shows a repeating pattern, although not strictly periodic. Therefore, a simple folding of the light curve would not return an accurate representation of the variability that we observe. On the other hand, the relatively low flux of this source requires some sort of averaging to allow a more accurate data analysis to be

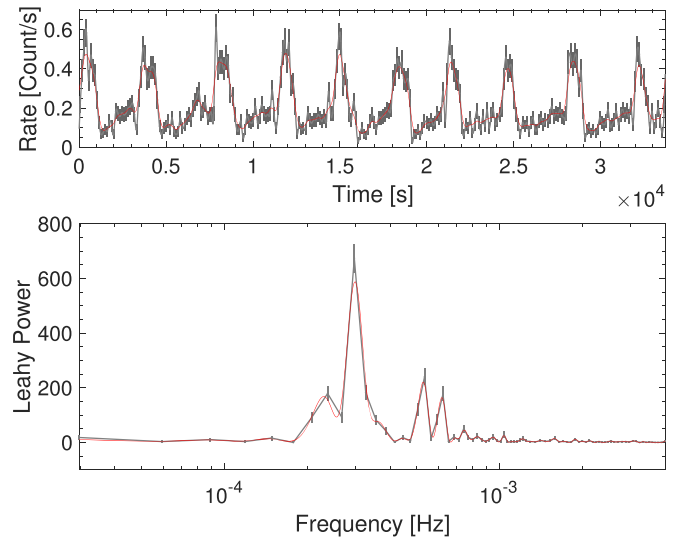


**Figure 1.** XMM-Newton data from 4X J1118. Top panel: light curve extracted combining the events collected with all EPIC cameras. Bottom panel: PDS calculated from the same data. In both panels, the actual data and their uncertainties (in gray) were smoothed using a Gaussian filter for clarity (red solid line).

performed. We created a folded light-curve profile following the approach of Neilsen et al. (2011), who applied it to GRS 1915+105. We first constructed a first-guess template model defining a representative single light-curve cycle. We then cross-correlated the template with the entire light curve, which comprises nine peaks. The resulting cross-correlation returns nine maxima that correspond to the peak in the light curve, and are assigned phase zero ( $\phi = 0$ ) in the construction of the folded profile. We then split the cross-correlation function in 20 phase bins, over which we phase-average the

**Table 2**  
Properties of the QPOs Detected in the EPIC-pn and MOS data from 4XMM J111816.0–324910

Instrument	Component	Frequency (Hz)	$Q$ factor	Significance ( $\sigma$ )
EPIC-pn	Main peak	$(3.022 \pm 0.003) \times 10^{-4}$	17.9	11.9
	Left shoulder	$(2.22^{+0.01}_{-0.01}) \times 10^{-4}$	unresolved	5.4
	Secondary peak 1	$(5.2 \pm 0.1) \times 10^{-4}$	unresolved	6.8
	Secondary peak 2	$(7 \pm 2) \times 10^{-4}$	unresolved	5.9

**Note.** The main peak is the most prominent peak in the PDS from both the EPIC-pn and MOS data. The secondary peaks 1 and 2 are the two peaks visible on the right-hand side of the main peak. The left shoulder is the low-amplitude feature visible at the left-hand side of the main peak, and only detected in the EPIC-pn data. Uncertainties are given at a  $1\sigma$  level.

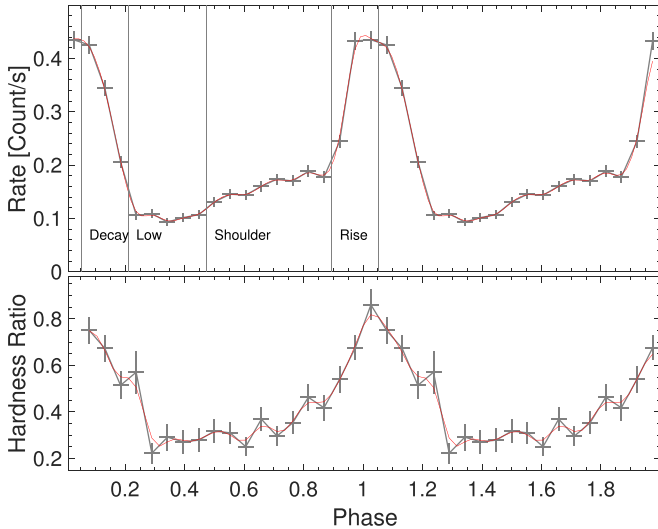


**Figure 2.** Top panel: EPIC phase-folded light curve, in the 0.3–10 keV band. The phase intervals used for the phase-resolved spectroscopy are marked by vertical lines. Bottom panel: Hardness ratio between the fluxes obtained in the 0.3–2 keV and 2–10 keV bands, respectively. As in Figure 1 the actual data were smoothed using a Gaussian filter for clarity.

original light curve. We then use the resulting profile as a new template, which we cross-correlate with the original light curve. The process is then iterated 10 times in order to minimize the bias introduced with the choice of our first-guess template. We applied the above method to the three light curves we extracted, and we used the light curves in the 0.3–2.0 and 3.0–10 keV bands to calculate a hardness ratio. The final phase-folded light-curve extracted for the 0.3–10 keV band and the hardness ratio as a function of phase are shown in Figure 2 (top and bottom panels, respectively). The profiles shown correspond to an average period of approximately 3500 s.

In the following, uncertainties will be given at  $1\sigma$ , with the exception of the spectral results, where uncertainties are quoted at a 90% confidence level.

## 2.2. Spectral Analysis

We first extracted the three (one EPIC-pn and two EPIC-MOS) average spectra in the 0.3–10 keV energy range from the entire observation. The appropriate ancillary and response files were created with the SAS package. Then, in order to probe the fast variability of the target along the repeated pattern that characterizes the light curve, we extracted four spectra in the 0.3–10 keV energy range at different phases of said pattern, following the folded profile obtained as described above. We

extracted four spectra, labeled low, shoulder, rise, and decay, in the phase ranges shown in Figure 2 (top panel).

## 3. Results

### 3.1. Timing Results

The PDS from 4X J1118 shows a prominent main peak at  $(3.02 \pm 0.03) \times 10^{-4}$  Hz, clearly corresponding to the obvious high-amplitude  $\approx 3500$  s modulation visible in the light curve. Such a peak is detected with high statistical significance ( $15.3\sigma$ ) and has a quality factor  $Q = 18$ .<sup>9</sup> The PDS shows two additional secondary peaks, at  $(5.2 \pm 0.1) \times 10^{-4}$  Hz and  $(7 \pm 2) \times 10^{-4}$  Hz ( $9.2$  and  $7.6\sigma$ , respectively), although they are both unresolved (i.e., their FWHM is significantly lower than our frequency resolution of  $\sim 3 \times 10^{-5}$  s). A relatively low-amplitude peak at  $(2.22 \pm 0.01) \times 10^{-4}$  Hz ( $7.2\sigma$ ) is also detected. While the peak at  $6 \times 10^{-4}$  Hz is consistent with being harmonically related to the prominent main peak, both the peaks at 5.2 and  $2.22 \times 10^{-4}$  Hz do not appear to be in any obvious harmonic relation with the main peak, and cannot be obviously associated with a particular feature in the light curve. Further in-depth analysis of the above features is beyond the scope of this work. The main best-fit parameters are listed in Table 2.

For the sake of comparison, we analyzed a representative RXTE observation of GRS 1915+105 (Obs. ID 60405-01-02-00) during which the heartbeats were clearly observed. The flare modulation occurs on an average period of 50 s, and—similarly to 4X J1118—is clearly visible as a prominent peak in the PDS. The PDS also shows two secondary peaks, qualitatively similar to those observed in the PDS from 4X J1118. In this case, however, both peaks are consistent with being harmonically related to the main peak, forming a 1–2–3 harmonic series.<sup>10</sup> We note that this is only a representative case, and that GRS 1915+105 shows similar modulations at a variable period, which can be as long as  $\sim 1000$  s (Belloni et al. 2000; Altamirano et al. 2011; Weng et al. 2018). Hence, the properties of the PDS change in time, and the harmonic relation highlighted above is not always observed nor consistently respected.

The 4X J1118 profile that emerges in its folded light curve has a clear structure, formed by a main peak, consistent with being symmetrical and best-described by a Gaussian function; a left shoulder, preceding the peak; a low-flux phase, corresponding to the minimum flux level reached during the duty cycle, following the main peak. Based on the above, we can estimate a number of

<sup>9</sup> The quality factor  $Q$  quantifies the coherence of a given signal and is defined as  $Q = \nu/\Delta\nu$ , where  $\nu$  and  $\Delta\nu$  are the centroid frequency and the FWHM of the peak, respectively.

<sup>10</sup> Note that while third harmonics are not unheard of in accreting BH binaries (see, e.g., Motta et al. 2017), they remain puzzling and their origin widely debated.

**Table 3**  
Best Fits of the Four Phase-resolved Spectra

Model	Parameter	Low	Shoulder	Rise	Decay	$\chi^2_\nu/\text{dof}$
diskbb	$N_{\text{H}}$ ( $10^{20}$ cm $^{-2}$ )			$4^{+2}_{-1}$		1.11/221
	$kT$ (keV)	$0.80^{+0.1}_{-0.09}$	$1.06^{+0.08}_{-0.08}$	$2.3^{+0.3}_{-0.2}$	$1.8^{+0.2}_{-0.2}$	
	Norm. ( $10^{-3}$ )	$23^{+13}_{-8}$	$14^{+5}_{-3}$	$2.8^{+1}_{-0.8}$	$4.9^{+1}_{-1}$	
	$L$ ( $10^{39}$ ) <sup>a</sup>	$1.0^{+0.1}_{-0.1}$	$2.0^{+0.1}_{-0.1}$	$7.4^{+0.6}_{-0.6}$	$5.9^{+0.5}_{-0.5}$	
diskpbb	$N_{\text{H}}$ ( $10^{20}$ cm $^{-2}$ )			$15^{+4}_{-4}$		0.96/219
	$kT$ (keV)	$1.2^{+0.6}_{-0.3}$	$2.3^{+1.9}_{-0.7}$	$3.5^{+4.6}_{-0.9}$	$2.4^{+0.8}_{-0.4}$	
	$p$		$0.53^{+0.04}_{-0.03}$		$0.63^{+0.04}_{-0.03}$	
	Norm. ( $10^{-4}$ )	$16^{+30}_{-10}$	$2^{+9}_{-2}$	$3^{+9}_{-3}$	$11^{+20}_{-8}$	
	$L$ ( $10^{39}$ ) <sup>a</sup>	$1.3^{+0.2}_{-0.2}$	$2.7^{+0.3}_{-0.3}$	$8.3^{+0.8}_{-0.7}$	$6.6^{+0.7}_{-0.6}$	
bbody+diskbb	$N_{\text{H}}$ ( $10^{20}$ cm $^{-2}$ )			$10^{+3}_{-3}$		0.93/220
	$kT_{\text{bbody}}$ (keV)			$0.24^{+0.04}_{-0.03}$		
	Norm. ( $10^{-7}$ )			$10^{+12}_{-8}$		
	$L_{\text{bbody}}$ ( $10^{38}$ ) <sup>a</sup>			$4.1^{+0.9}_{-0.9}$		
	$kT_{\text{diskbb}}$ (keV)		$1.4^{+0.2}_{-0.2}$		$2.5^{+0.4}_{-0.3}$	$2.0^{+0.3}_{-0.2}$
	Norm. ( $10^{-3}$ )	$1.8^{+1}_{-0.9}$		$4^{+3}_{-2}$	$1.9^{+1}_{-0.7}$	$4^{+2}_{-1}$
	$L_{\text{diskbb}}$ ( $10^{39}$ ) <sup>a</sup>	$0.8^{+0.1}_{-0.2}$		$1.8^{+0.2}_{-0.2}$	$7.5^{+0.6}_{-0.6}$	$5.6^{+0.5}_{-0.5}$

**Notes.** Errors are quoted at a 90% confidence level for each parameter of interest.

<sup>a</sup> Unabsorbed 0.3–10 keV luminosity.

timescales that characterize the variability in 4X J1118. We stress that the repeated pattern in the light curve is not strictly periodic, and therefore the timescales in the following have to be intended as average quantities. The average recurrence time of the flaring observed in the light curve is  $T_{\text{rec}} \approx 3500$  s. The flares are consistent with being almost symmetric, and have a duration of  $T_{\text{dur}} \approx 700$  s, which is defined as the FWHM of the Gaussian that best fits the main peak of the folded light curve. The average flare rise and decay are equal to  $T_{\text{rise}} \approx 350$  s and  $T_{\text{decay}} \approx 525$  s, respectively. We defined  $T_{\text{rise}}$  as the interval between the intersection of the Gaussian that best fits the flare and the shoulder preceding the flare itself, and the Gaussian peak. The decay is defined as the interval between the peak of said Gaussian profile and the first point of the plateau following the flare (around  $\phi = 0.2$ ). We note that the  $T_{\text{rise}}$  and  $T_{\text{decay}}$  timescales do not exactly coincide with the phase ranges we defined to perform the phase-resolved spectroscopy (where the limited signal-to-noise ratio imposed a less accurate event selection with respect to that adopted for the timing analysis).

### 3.2. Spectral Results

The EPIC average energy spectra are well-fit by a number of models, which include a blackbody (bbody), a disk-blackbody (diskbb), and a power law or a bremsstrahlung profile (bremss), all modified by a component accounting for the absorption by the inter-stellar medium (tbabs, using the abundances by Wilms et al. 2000). Unsurprisingly, combinations of the above models or similar ones (such as diskpbb or Comptonization models, e.g., nthcomp; Zdziarski et al. 1996) also provide acceptable fits. For example, an absorbed diskbb yields a  $\chi^2_\nu = 1.13$  for 267 degrees of freedom (dof), with the following parameters:  $N_{\text{H}} = (3.0 \pm 1.0) \times 10^{20}$  cm $^{-2}$ ,  $kT = 1.6 \pm 0.7$  keV, and an observed 0.3–10 keV flux of  $(5.9 \pm 0.2) \times 10^{-13}$  erg cm $^{-2}$  s $^{-1}$ . For an absorbed diskpbb ( $\chi^2_\nu/\text{dof} = 0.95/266$ ) we obtained  $N_{\text{H}} = (1.3 \pm 0.3) \times 10^{20}$  cm $^{-2}$ ,  $kT = 2.4^{+0.5}_{-0.3}$  keV, and  $p = 0.59 \pm 0.02$ , providing an absorbed flux of  $(6.2 \pm 0.3) \times 10^{-13}$  erg cm $^{-2}$  s $^{-1}$ . For a distance of 6.7 Mpc, the inferred

average luminosity is  $(3.24 \pm 0.08) \times 10^{39}$  and  $(3.7 \pm 0.1) \times 10^{39}$  erg s $^{-1}$  for the diskbb and diskpbb model, respectively. Also an absorbed cutoff power law ( $\chi^2_\nu = 0.97/256$ ) provides an acceptable fit, with  $N_{\text{H}} = (1.1 \pm 0.3) \times 10^{21}$  cm $^{-2}$ , photon-index  $\Gamma = 1.1 \pm 0.2$ , high-energy cutoff  $E_{\text{high}} = 5^{+2}_{-1}$ , and an observed 0.3–10 keV flux of  $(6.1 \pm 0.3) \times 10^{-13}$  erg cm $^{-2}$  s $^{-1}$ . However, since the disk models appear to provide slightly better results, in the following we will only consider fits based on diskbb and diskpbb models.

The hardness ratio in Figure 2 (bottom panel) clearly shows that the variability in 4X J1118 is associated with marked spectral variations, with spectra becoming harder any time the flux peaks. Therefore, the above values have to be intended only as rough estimates that reflect the general (and approximate) spectral properties of 4X J1118. Phase-resolved spectroscopy doubtlessly constitutes a more suitable approach to probe the spectral properties of our target. Hence we analyzed the EPIC-pn and MOS spectra of 4X J1118 in four phase ranges, labeled as low, shoulder, rise, and decay (see Figure 2, top panel).

As for the average spectrum, phenomenological models such as an absorbed power law, a diskbb, or a diskpbb, all provide adequate fits to the individual phase interval spectra, and return significantly varying flux and parameters. Fitting simultaneously the spectra with a diskbb, leaving free to vary both the disk temperature and its normalization for each phase range while keeping a common column density, provides an acceptable fit ( $\chi^2_\nu/\text{dof} = 1.10/221$ ; Table 3), which, however, retains some structured residuals to the data (see Figure 3, middle panel). According to this model, the disk unabsorbed bolometric luminosity correlates with the inner disk temperature, following a  $L \sim T^{(1.97 \pm 0.01)}$  relation (see Figure 3, right panel). Interestingly, a relation of the form  $L \sim T^2$  is expected for a slim disk. The deviations of a slim disk from a standard disk-blackbody might thus be at the origin of the structured residuals that we observe.

Based on the above consideration, we substituted the diskbb with a diskpbb model, where the radial dependence of the disk



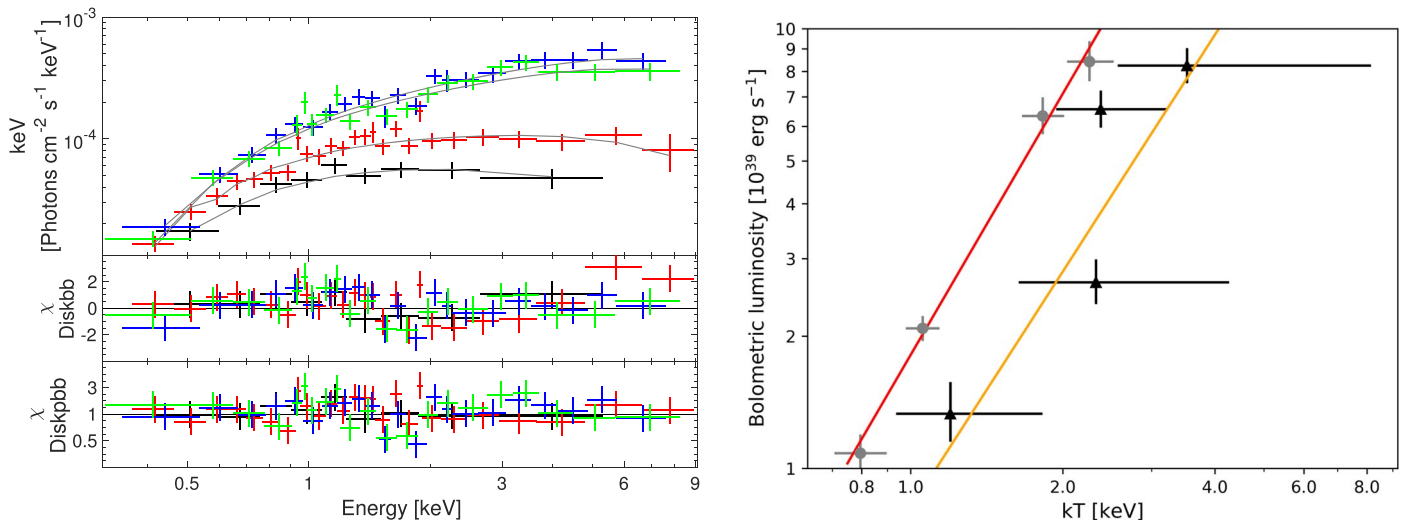


**Figure 3.** Left: unfolded XMM-Newton spectra of the phase-resolved epochs fitted with a diskbb model. Colors mark different phases: black is low, red is shoulder, blue is rise, and green is decay. Data were rebinned for the purpose of display only. For clarity, we show only the EPIC-PN spectra. Right: disk luminosity as a function of the temperature for the diskbb (gray points) and diskpbb (black triangles) models fitted with  $L \propto T^{1.97 \pm 0.01}$  (red solid line) and  $L \propto T^{1.8 \pm 0.7}$  (yellow solid line), respectively.

temperature has a power-law profile of the form  $r^{-p}$ , with  $p = 3/4$  for a standard disk and  $p = 1/2$  for a slim disk. When fitting this model to the data, we linked the  $p$  parameter across the two spectra at higher flux, and across the two spectra at lower flux, respectively. This configuration returns a good description of the spectra, slightly preferred by the data with respect to the previous model ( $\chi^2/\text{dof} = 0.96/219$ , see Table 3 and Figure 3, top panel for the best-fit and bottom panel for the model residuals), with a  $p$ -parameter of  $0.63 \pm 0.04$  and  $0.53 \pm 0.04$  for the high and the low-flux spectra, respectively. The disk temperature for the four phase ranges lies between 1 and 4 keV, although the values are less constrained than in the previous fits. Using this model, we obtain a luminosity–temperature relation of the form  $L \sim T^{(1.8 \pm 0.7)}$ , which is fully consistent with the relation expected in the presence of a slim disk. A rough estimate of the range of the inner radii from the diskpbb model normalization lies at  $\approx 15\text{--}40$  km, adopting an inclination angle of  $60^\circ$  and with no color correction applied. These values must be taken as merely indicative, as they clearly do not reflect the actual disk truncation radii, but rather suggest that the truncation radius may change with varying flux. The simplified models we adopted may not fully describe the complex spectral variations observed in 4X J1118, but the limited signal-to-noise ratio and the lack of data at high energies of our spectra does not allow us to test more sophisticated models.

Finally, we considered the typical spectral modeling employed to explain the ULX phenomenology, which explicitly assumes super-Eddington accretion around a stellar mass compact object (either a BH or a neutron star, NS). In such a scenario, at least two main spectral thermal components are identified: a cold one that is usually associated with extended and optically thick winds (launched by the super-Eddington disk), and a hot one ascribed to an advection-dominated disk (e.g., Middleton et al. 2015). We attempted to model the spectra of 4X J1118 with a cold blackbody plus a hot diskbb component.<sup>11</sup> Since limited variability is expected from the wind due to its large radial extension

(Middleton et al. 2015), we linked both the column density and the blackbody parameters across the four phases, while we left the diskbb parameters free to vary. This model provides a good fit of the data ( $\chi^2/\text{dof} = 0.9/220$ ), which gives a column density of  $(1.0 \pm 0.3) \times 10^{21} \text{ cm}^{-2}$  and cold blackbody temperature of  $0.24 \pm 0.04$  keV, with an emitting radius of  $1000 \pm 350$  km. The hot diskbb components gives a common temperature of  $1.4 \pm 0.2$  keV for the low and shoulder spectra, while for the rise and decay we obtained a temperature of  $2.5_{-0.3}^{+0.4}$  keV and  $2.0_{-0.2}^{+0.3}$  keV, respectively. Based on the diskbb fits, assuming no color correction factor and a disk inclination of  $60^\circ$ , the inner radii are  $40_{-11}^{+14}$  km,  $60_{-15}^{+18}$  km,  $42_{-9}^{+9}$  km, and  $56_{-10}^{+12}$  km, for the low, shoulder, rise, and decay spectra, respectively.

#### 4. Other X-Ray Observations

The field of 4X J1118 was observed with Chandra, Swift, and NuSTAR (largely overlapping with the XMM-Newton observation; see Table 1).

In 2008, Chandra caught the source at a rather low luminosity. Since the Chandra observation does not provide enough counts for a meaningful spectral analysis, in order to estimate the luminosity from the count rate we arbitrarily assumed that the spectrum is described by a blackbody with temperature of 0.4 keV, which is the temperature we obtain by fitting a blackbody model to the low spectrum. We obtain a luminosity of  $\approx 4 \times 10^{37} \text{ erg s}^{-1}$  (consistent values are obtained with other plausible models, for example,  $\approx 6 \times 10^{37} \text{ erg s}^{-1}$  adopting a power-law model with slope  $\Gamma = 2$ ).

4X J1118 was never convincingly detected in the Swift exposures, due to the presence of contaminating sources very close to the target’s fiducial position in the Swift images, as well as of diffuse X-ray emission from NGC 3261. The deepest Swift upper limits are of the order of  $8 \times 10^{38} \text{ erg s}^{-1}$  ( $10^{-3}$  XRT counts  $\text{s}^{-1}$  correspond to  $\approx 1.3 \times 10^{38} \text{ erg s}^{-1}$ ).

In the NuSTAR data 4X J1118 is detected with a significance exceeding  $5\sigma$  up to 15–20 keV. We extracted the background-subtracted 3–15 keV light curve, combining the data from the NuSTAR/FMPA and NuSTAR/FMPB instruments. The light

<sup>11</sup> A diskpbb component would be more adequate for such a scenario; however, the data quality does not allow us to put firm constraints on the parameters of this model.

curve shows flares similar to those observed in the XMM-Newton data, which appear to occur at the same time when NuSTAR and XMM-Newton were observing at the same time. However, due to the low signal-to-noise ratio of the data, the contamination from a nearby ( $\sim 30''$ ) bright source, and the orbit gaps, we refrained from using the NuSTAR data for the spectral or timing analysis.

## 5. Discussion

The high Galactic latitude of this source and the faint optical counterparts (see Figures B1 and B2 in Appendix B) make an association of 4X J1118 with a foreground X-ray source (such as a CV or a polar) quite unlikely. We thus approach 4X J1118 as a new ULX, which enriches the still small population of known transients within this class.

The most striking feature of 4X J1118 is the similarity of its light curve with that of the Galactic BH binary GRS 1915+105 in one of its many variability states: the  $\rho$  class variability (Belloni et al. 2000), sometimes affectionately referred to as the heartbeats, which is characterized by a quasi-periodic modulation in the flux. Such marked short timescale variability is clearly at odds with most of the ULXs, where only a small sample of sources is highly variable on timescales shorter than a few hours (e.g., Earnshaw & Roberts 2017; Pintore et al. 2020). 4X J1118 can be classified as a broadened-disk or hard-ultraluminous source (Sutton et al. 2013), and, by showing both relatively hard spectra and obvious variability, may depart from the common variable-when-softer connection observed in other ULXs (Sutton et al. 2013; Middleton et al. 2015).

Aside from GRS 1915+105, a few more objects at times show a  $\rho$ -like variability: IGR J17091–3624, MXB 1730–335, and the AGN in GSN 069. IGR J17091–3624 is thought to be powered by a stellar mass BH, and is considered a fainter relative of GRS 1915+105, with which it shares many characteristic variability patterns (Altamirano et al. 2011). MXB 1730–335, also known as the Rapid Burster, has been recently shown to display—among many other variability patterns—two of the many characteristic variability classes observed in GRS 1915+105 (the  $\rho$  and  $\theta$  class, see Bagnoli & in’t Zand 2015), despite hosting a confirmed NS (Hoffman et al. 1978). GSN 069, which is powered by a supermassive BH with a mass of the order of  $\sim 10^5 M_\odot$ , recently started to show a flux modulation reminiscent of the heartbeats (Miniutti et al. 2019). Such a modulation, unsurprisingly, occurs with a much longer periodicity than in GRS 1915+105 (approximately 9 hr), ascribed to the large mass of this object.

When compared in some detail, the light curves of 4X J1118, GRS 1915+105, IGR J17091–3624, and the Rapid Burster, all show the same structure, constituted by a low-flux plateau, a shoulder, and a main peak, the latter typically asymmetric, with a slower rise to the peak (in our case equivalent to the sum of the time interval covering the shoulder and  $T_{\text{rise}}$ ) and a fast decay. In this matter, GSN 069 represents an exception, with its very symmetric peaks and nondetectable pre-peak shoulder. What clearly differentiates these qualitatively similar light curves is the recurrence time of the main peaks. From fastest to slowest, the recurrence times are  $\sim 5$ – $100$  s (IGR J17091–3624),  $40$ – $1000$  s (GRS 1915+105),  $\sim 350$ – $450$  s (Rapid Burster),  $\sim 3200$ – $3700$  s (4X J1118), and  $\approx 32.5$  ks (GSN 069).

The soft X-rays spectrum (below 10 keV) at the time of the heartbeat in 4X J1118 appears to be thermal, with the emission well-modeled by a disk-like component, and relatively hard. Our

best fits to the phase-resolved spectra of 4X J1118 indicate that both the disk temperature and the inner disk truncation radius vary across different phases, but while the former clearly increases with flux, our data do not allow us to make a conclusive statement on the evolution of the inner disk radius. Similar properties have been observed in all the aforementioned sources (which—we remind the reader—include an NS and a BH Galactic X-ray binary, as well as a supermassive BH), with the addition that in all these sources the inner disk radius consistently increases with flux during the heartbeats. In particular, in GRS 1915+105—the first source to have shown this particular variability state—the above spectral behavior has been interpreted as the result of a limit-cycle instability driven by the Lightman–Eardley radiation pressure instability (Lightman & Eardley 1974; Belloni et al. 2000). An excess density wave propagates in the innermost portion of the accretion disk, eventually inducing local Eddington accretion that causes the flux to peak, while the accretion disk reacts by increasing its truncation radius at an almost constant temperature. Our results are consistent with this picture, although the limited statistical quality of our data does not allow us to make any stronger statement. The radiation pressure limit-cycle instability has been invoked to explain the heartbeats also in IGR J17091–3624 (Altamirano et al. 2011), GSN 069 (Miniutti et al. 2019), and even in the Rapid Burster, where the instability might develop in a portion of the accretion flow unaffected by type-I X-ray bursts eventually emitted from the NS surface (see Maselli et al. 2018).

The fits to the phase-resolved spectra return a relation between bolometric luminosity versus disk temperature of the form  $L \propto T^p$ , where  $p \approx 2$ , which indicates that the accretion disk around 4X J1118 is likely a slim disk. A similar power-law relation has been found by Miniutti et al. (2019) for GSN 069, who found a luminosity–temperature relation with index  $p = 4$ . For what concerns GRS 1915+105 and IGR J17091–3624, a comparison with 4X J1118 is much more difficult: possibly due to the much better signal-to-noise ratio of the data from these sources, and/or a much larger amount of data available, it appears that in either sources there is no interval longer than a few seconds over which  $L \propto T^4$  (or any other power-law relation with constant index). Rather, both sources trace hysteresis cycles in the luminosity versus temperature plane with  $p$  varying in the 2–4 range (but in opposite directions), reflecting a complicated accretion scenario (Altamirano et al. 2011; Court et al. 2017; Maselli et al. 2018). In the case of the Rapid Burster, it is unclear whether a correlation between disk temperature and luminosity exists in the first place, as the disk temperature during the heartbeats seems to remain roughly constant in time (Bagnoli & in’t Zand 2015).

Among the sources showing heartbeats considered here, both a mass and a distance estimate are available for GRS 1915+105 ( $M \approx 12 M_\odot$ ,  $d \approx 8.6$  kpc; Reid et al. 2014), for the Rapid Burster ( $M \approx 1.5 M_\odot$ ,  $d \approx 8$  kpc; Lewin et al. 1976), and for GSN 069 ( $M \approx 4 \times 10^5 M_\odot$ ,  $z \approx 0.018$ ; Miniutti et al. 2019). This made it possible to establish that the heartbeats occur at  $\sim 80\%$ – $90\%$  of the source Eddington luminosity ( $L_{\text{Edd}}$ ) in GRS 1915+105, between 40 and 90%  $L_{\text{Edd}}$  in GSN 069, and only at  $\approx 20\%$  in the Rapid Burster (Neilsen et al. 2011; Bagnoli & in’t Zand 2015; Miniutti et al. 2019). On the one hand, this suggests that Eddington accretion rates might not be a necessary condition for the heartbeats to occur, a fact already noted by many authors and also supported by hydrodynamical simulations (see,

e.g., Janiuk et al. 2015). On the other hand, the above observation implies that we cannot easily assume that 4X J1118 is accreting at close-to-Eddington rates by comparison with, e.g., GRS 1915+105. This fact becomes even more striking when we consider that while GRS 1915+105, IGR J17091–3624, the Rapid Burster, and GSN 069 undoubtedly show similar heartbeats’ light curves and spectral properties, all these sources (and especially the three stellar-mass systems) also show a large variety of widely unexplained additional variability states. Therefore, without more observations, better signal-to-noise, and more in-depth studies, we are not in a position to exclude that all the similarities that we have identified among the above sources are purely coincidental.

We are now left with the daunting task of discussing the possible nature of the compact object hosted in 4X J1118. Having excluded the obvious presence of type-I X-ray bursts in our X-ray data by visual inspection of the data, we performed an accelerated search for coherent signals in the XMM-Newton observation, which did not reveal any significant feature (see Appendix A for details on the analysis). Therefore, we have no direct proof of the presence of a surface, which would unquestionably indicate the presence of an NS. Our spectral analysis does not offer any insight into this matter either, as no clear similarity or difference between 4X J1118 and either the Rapid Burster (hosting a confirmed NS) or any of the other systems we considered (all hosting confirmed or candidate BHs) has emerged. Our only option is to attempt a mass estimate of the compact object based on the information we have on 4X J1118, aware of the fact that the mass of the accreting object might not be the dominant factor that determines its variability timescale (see, e.g., Massaro et al. 2020a, 2020b, for a case study on GRS 1915+105). We identified three different ways to do this, all depending on fairly strong assumptions, and thus limited by important caveats.

First, by assuming that the maximum luminosity reached by 4X J1118 equals its Eddington limit (which is not necessarily a sensible assumption, as discussed above) based on our spectral analysis we obtain a mass of approximately  $75 M_{\odot}$ . By assuming that 4X J1118 is accreting at 10 times the Eddington accretion rate instead—which is not unusual in NS powered ULXs (see, e.g., Israel et al. 2017)—this mass moves down to  $7.5 M_{\odot}$ , a value comfortably consistent with the average expected mass of BHs in Galactic binary systems (Özel et al. 2010). Second, we observe that all the most relevant timescales in accreting systems (e.g., the viscous, thermal, and perturbation propagation timescales) are proportional to the dynamical timescale,  $t_{\text{dyn}} \approx \frac{GM}{c^3} r^{3/2}$ , where  $r$  is expressed in units of the gravitational radius  $R_g = GM/c^2$ . If we make the (strong) assumptions that the heartbeats arise from the same portion of the accretion flow in two sources, and that the two accretion flows have the same characteristics (e.g., same disk scale height  $H/R$  and viscosity parameter  $\alpha$ ), we obtain that any characteristic timescale simply scales linearly with the mass of the object.<sup>12</sup> Taking  $M = 10 M_{\odot}$  for GRS 1915+105, and a recurrence time of 100 s and 3500 s, respectively, for GRS 1915+105 and 4X J1118, it follows that 4X J1118 should have a mass of the order  $M \approx 350 M_{\odot}$ . It is immediately clear, however, that such a rough estimate is strongly sensitive to the choice of (i) the characteristic timescale used, which can vary significantly even for one single object (up to 3 orders of

magnitude for, e.g., IGR J17091–3624 and GRS 1915+105); and (ii) the object used for the comparison (e.g., GRS 1915+105 as opposed to the Rapid Burster or GSN 069). This indicates that our assumptions are most likely too simplistic, and the above mass estimate can easily vary by orders of magnitude depending on our relatively arbitrary choices. Finally, we can attempt a mass estimate by assuming that the heartbeats recurrence times are governed by the radiation-pressure limit-cycle instability. We followed the approach adopted by Miniutti et al. (2019) and we used an empirical relation derived from numerical simulations of AGN that links the BH mass, the instability recurrence time, and the ratio  $A$  between the minimum and maximum luminosity sampled during the instability duty cycle—that is,  $M_{\text{BH}} = 0.45 T_{\text{rec}}^{0.87} A^{-0.72} (\alpha/0.02)^{1.88}$  (Janiuk et al. 2004)—to compare once more 4X J1118 and GRS 1915+105. By making the same assumptions as above on the accretion flow, and taking  $A = 0.3$  for GRS 1915+105 (based on Neilsen et al. 2011), and  $A = 0.13$  from this work for 4X J1118, we find that the latter should have a mass of the order  $M \approx 400 M_{\odot}$ . As mentioned above, it is unlikely that  $\alpha$ ,  $H/R$ , and the size of the portion of the accretion flow generating the heartbeats are the same for 4X J1118 and GRS 1915+105 (or any other system that might be used for comparison). It follows that, once more, the above mass estimate is not really constraining, as it strongly depends on our assumptions.

Based on all the above considerations, we cannot make a strong statement on the nature of the compact object in 4X J1118, which might very well be a stellar-mass BH as well as an NS, or even a more exotic intermediate-mass BH. We believe the latter possibility less likely, as the existence of an intermediate-mass BH would be difficult to explain in terms of galactic evolution and dynamics in a galaxy powered by a relatively light supermassive BH, and lacking any clear sign of interaction with other galaxies.

Clearly, the marked variability observed in 4X J1118 may be due to a number of processes different from the radiation-pressure limit-cycle instability, and not necessarily instability driven (see, e.g., Middleton et al. (2018) for a number of possibilities involving precession, and Bagnoli et al. (2015) for a list of magnetic models). However, the fact that we are currently unable to constrain the mass of the accreting object in this source prevents us from making any meaningful comparison between its observed variability and that predicted by essentially any existing model. New observations and more data are needed in order to clarify what physical processes might underlie the observed properties of 4X J1118.

We thank the anonymous referee for helpful comments that contributed to improving this work. This research has made use of data produced by the EXTraS project, funded by the European Union’s Seventh Framework Programme under grant agreement No. 607452. The scientific results reported in this article are based on observations obtained with XMM-Newton, an ESA science mission with instruments and contributions directly funded by ESA Member States and NASA. This work was supported by the Oxford Centre for Astrophysical Surveys, which is funded through generous support from the Hintze Family Charitable Foundation. We acknowledge funding in the framework of the ASI-INAF contract n. 2017-14-H.0 and of the PRIN MIUR 2017 “UnIAM (Unifying Isolated and

<sup>12</sup> This is because both the radius and the accretion flow parameters  $H/R$  and  $\alpha$  can be eliminated from the equations when comparing timescales, because they are assumed to be constant across the sources considered.

Accreting Magnetars).” We acknowledge the INAF computing center of Osservatorio Astrofisico di Catania for the availability of computing resources and support under the coordination of the CHIPP project.

*Facilities:* XMM-Newton (EPIC), Swift (XRT), Chandra (ACIS), NuSTAR, HST (ACS).

*Software:* SAS (Gabriel et al. 2004), FTOOLS (Blackburn 1995), XSPEC (Arnaud 1996), CIAO (Fruscione et al. 2006).

### Appendix A Search for Rapid Pulsations

We considered the possibility of a fast-spinning pulsar in the system (see, e.g., Israel et al. 2017). For the XMM-Newton data set, after correcting the times to the solar system barycenter, we performed an accelerated search for signals by correcting the time of arrivals (ToA) of each photon in order to account for time shifts corresponding to those originated by a first period derivative component in the range  $|\dot{P}/P| < 10^{-6}$  Hz, and then by looking for peaks above a  $3.5\sigma$  local detection threshold in the corresponding power spectral density and taking into account the possible presence of non-Poissonian noise components (Israel & Stella 1996). We performed the search both over the whole sample of available ToA and only for those around the quasi-periodic peaks. The search gave negative results in both cases. No candidate signal was found in the 150 ms–100 s period range, with  $3\sigma$  upper limits in the 20%–30% and 50%–90% range for “all” the ToA and for the quasi-periodic oscillations (QPOs) “peaks,” respectively (see Figure A1).

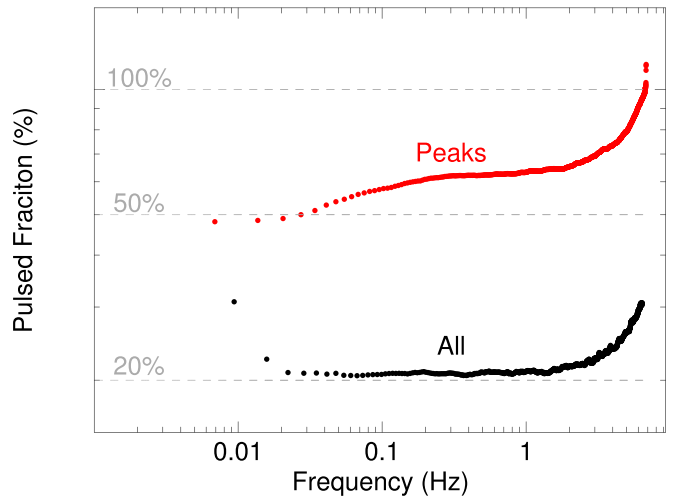


**Figure A1.** Upper limits on fast pulsations inferred from an accelerated search taking into account the possible presence of a first period derivative component  $\dot{P}$  and for two different cases: “All” including all the source events and “Peaks” only for the brightest intervals of the QPOs. In the former case we inferred 20%–30% pulsed fraction at  $3\sigma$  between 150 ms and 100 s, and about 50%–90% pulsed fraction for the “Peaks.”

### Appendix B Hubble Space Telescope Observations

NGC3621 was observed with the HST/ACS instrument in the F435W (*B*) filter, F555W (*V*) filter, and F814W (*I*) filter. We retrieved calibrated, geometrically corrected images from the Hubble Legacy Archive (HLA2). We refined astrometry



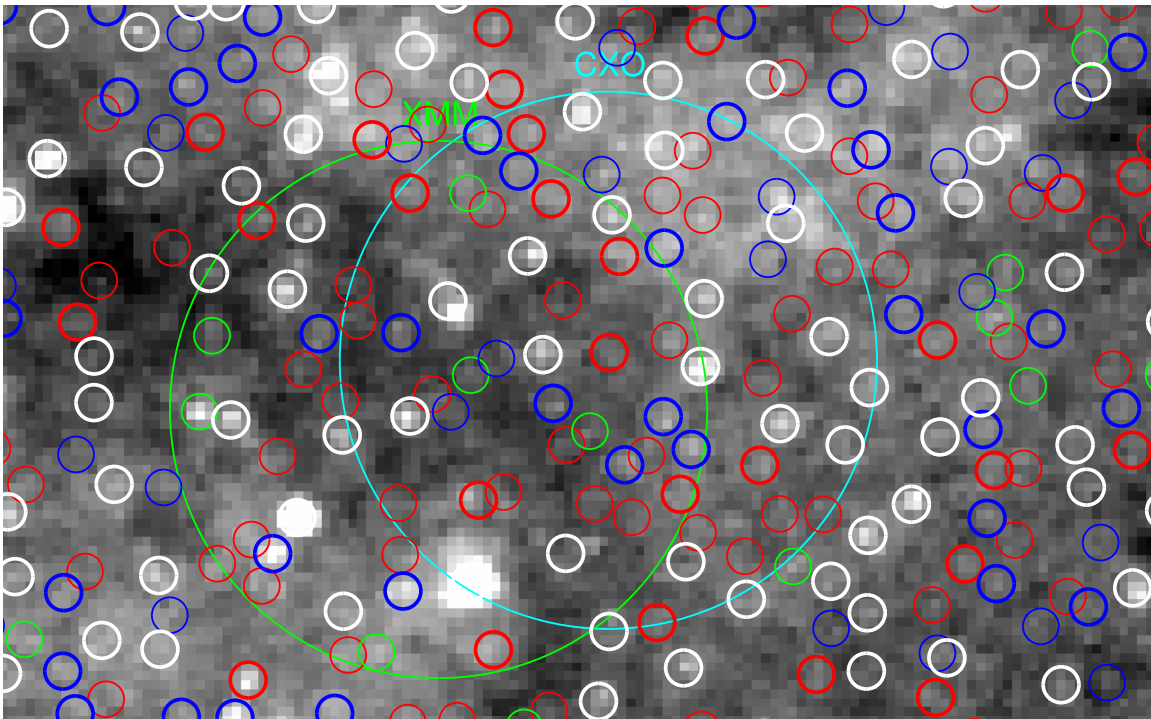


**Figure B1.** The field as seen by HST in the  $V$  band, with XMM-Newton and Chandra error circles superimposed (Chandra: 99% confidence level; XMM-Newton: 68% confidence level). White circles: HST sources detected in  $BVI$ ; bold blue:  $BV$ , not  $I$ ; bold red:  $VI$ , not  $B$ ; thin blue:  $B$  only; thin green:  $V$  only; thin red:  $I$  only.

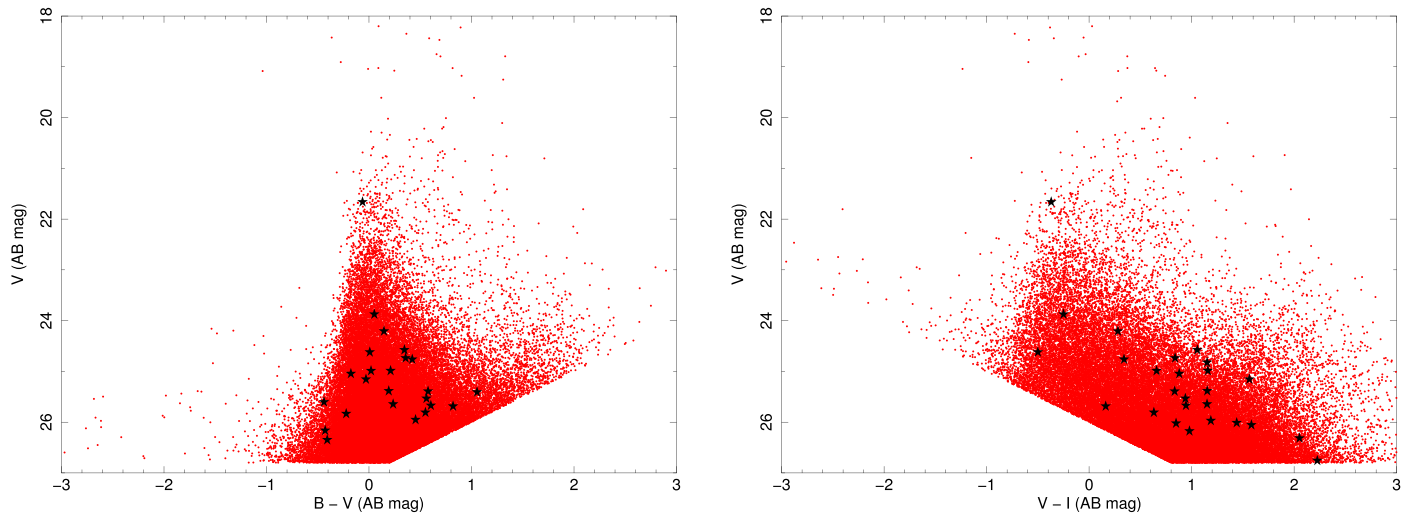





**Figure B2.** Left:  $B$  minus  $V$  vs.  $V$  color–magnitude diagram, based on sources detected in both filters. Sources lying in the Chandra error region are marked with black stars. Right: same as left figure, but  $V$  minus  $I$  color–magnitude diagram. In both panels we excluded all sources below AB mag 26.8, 27.0, and 26.0 in the  $B$ ,  $V$ , and  $I$  bands, respectively—such values being a robust estimate of the sensitivity limit of the images, based on the observation of the peak in the number count histogram of magnitudes of detected sources.

using a set of sources from the Two Micron All Sky Survey, with a resulting rms accuracy better than 50 mas per coordinate (Figure B1). We run a source detection using the SExtractor software and we converted count rates to magnitudes using the photometric calibration provided by the HLA pipeline.

The brightest source consistent with the Chandra error circle is extended, and it is very likely a star cluster in NGC 3621 (see Figure B2).

#### ORCID iDs

M. Marelli  <https://orcid.org/0000-0002-8017-0338>  
P. Esposito  <https://orcid.org/0000-0003-4849-5092>

R. Salvaterra  <https://orcid.org/0000-0002-9393-8078>  
A. Tiengo  <https://orcid.org/0000-0002-6038-1090>  
G. A. Rodríguez Castillo  <https://orcid.org/0000-0003-3952-7291>

#### References

- Altamirano, D., Belloni, T., Linares, M., et al. 2011, *ApJL*, 742, L17  
Araud, K. A. 1996, in ASP Conf. Ser. 101, *Astronomical Data Analysis Software and Systems V*, ed. G. H. Jacoby & J. Barnes (San Francisco, CA: ASP), 17  
Bagnoli, T., & in't Zand, J. J. M. 2015, *MNRAS*, 450, L52  
Bagnoli, T., in't Zand, J. J. M., D'Angelo, C. R., & Galloway, D. K. 2015, *MNRAS*, 449, 268

- Barth, A. J., Strigari, L. E., Bentz, M. C., Greene, J. E., & Ho, L. C. 2009, *ApJ*, **690**, 1031
- Belloni, T., Klein-Wolt, M., Méndez, M., van der Klis, M., & van Paradijs, J. 2000, *A&A*, **355**, 271
- Blackburn, J. K. 1995, in ASP Conf. Ser. 77, *Astronomical Data Analysis Software and Systems IV*, ed. R. A. Shaw, H. E. Payne, & J. J. E. Hayes (San Francisco, CA: ASP), 367
- Court, J. M. C., Altamirano, D., Pereyra, M., et al. 2017, *MNRAS*, **468**, 4748
- De Luca, A., Salvaterra, R., Tiengo, A., et al. 2016, *The Universe of Digital Sky Surveys* (Cham: Springer), 291
- Earnshaw, H. M., & Roberts, T. P. 2017, *MNRAS*, **467**, 2690
- Fruscione, A., McDowell, J. C., Allen, G. E., et al. 2006, *Proc. SPIE*, **6270**, 62701V
- Gabriel, C., Denby, M., Fyfe, D. J., et al. 2004, in ASP Conf. Ser. 314, *Astronomical Data Analysis Software and Systems (ADASS) XIII*, ed. F. Ochsenbein, M. G. Allen, & D. Egret (San Francisco, CA: ASP), 759
- Gliozzi, M., Satyapal, S., Eracleous, M., Titarchuk, L., & Cheung, C. C. 2009, *ApJ*, **700**, 1759
- Hoffman, J. A., Marshall, H. L., & Lewin, W. H. G. 1978, *Natur*, **271**, 630
- Israel, G. L., Belfiore, A., Stella, L., et al. 2017, *Sci*, **355**, 817
- Israel, G. L., & Stella, L. 1996, *ApJ*, **468**, 369
- Janiuk, A., Czerny, B., Siemiginowska, A., & Szczerba, R. 2004, *ApJ*, **602**, 595
- Janiuk, A., Grzedzielski, M., Capitanio, F., & Bianchi, S. 2015, *A&A*, **574**, A92
- Kaaret, P., Feng, H., & Roberts, T. P. 2017, *ARA&A*, **55**, 303
- Lewin, W. H. G., Doty, J., Clark, G. W., et al. 1976, *ApJL*, **207**, L95
- Lightman, A. P., & Eardley, D. M. 1974, *ApJL*, **187**, L1
- Maselli, A., Capitanio, F., Feroci, M., et al. 2018, *A&A*, **612**, A33
- Massaro, E., Capitanio, F., Feroci, M., et al. 2020a, *MNRAS*, **495**, 1110
- Massaro, E., Capitanio, F., Feroci, M., et al. 2020b, *MNRAS*, **496**, 1697
- Middleton, M. J., Fragile, P. C., Bachetti, M., et al. 2018, *MNRAS*, **475**, 154
- Middleton, M. J., Heil, L., Pintore, F., Walton, D. J., & Roberts, T. P. 2015, *MNRAS*, **447**, 3243
- Miniutti, G., Saxton, R. D., Giustini, M., et al. 2019, *Natur*, **573**, 381
- Motta, S. E., Rouco-Escorial, A., Kuulkers, E., Muñoz-Darias, T., & Sanna, A. 2017, *MNRAS*, **468**, 2311
- Neilsen, J., Remillard, R. A., & Lee, J. C. 2011, *ApJ*, **737**, 69
- Özel, F., Psaltis, D., Narayan, R., & McClintock, J. E. 2010, *ApJ*, **725**, 1918
- Pintore, F., Marelli, M., Salvaterra, R., et al. 2020, *ApJ*, **890**, 166
- Reid, M. J., McClintock, J. E., Steiner, J. F., et al. 2014, *ApJ*, **796**, 2
- Rosen, S. R., Webb, N. A., Watson, M. G., et al. 2016, *A&A*, **590**, A1
- Satyapal, S., Vega, D., Heckman, T., O'Halloran, B., & Dudik, R. 2007, *ApJL*, **663**, L9
- Sutton, A. D., Roberts, T. P., & Middleton, M. J. 2013, *MNRAS*, **435**, 1758
- Tully, R. B., Courtois, H. M., Dolphin, A. E., et al. 2013, *AJ*, **146**, 86
- Webb, N. A., Coriat, M., Traulsen, I., et al. 2020, arXiv:2007.02899
- Weng, S.-S., Wang, T.-T., Cai, J.-P., Yuan, Q.-R., & Gu, W.-M. 2018, *ApJ*, **865**, 19
- Wilms, J., Allen, A., & McCray, R. 2000, *ApJ*, **542**, 914
- Zdziarski, A. A., Johnson, W. N., & Magdziarz, P. 1996, *MNRAS*, **283**, 193